F. Auteri, M. Carini, D. Zagaglia, D. Montagnani, G. Gibertini, C.B. Merz, A. Zanotti
A Novel Approach for Reconstructing Pressure from PIV Velocity Measurements
Experiments in Fluids, Vol. 56, N. 2, 2015, 45 (16 pages)
doi:10.1007/s00348-015-1912-z

Experiments in Fluids manuscript No.
(will be inserted by the editor)

A novel approach for reconstructing pressure from PIV velocity measurements

F. Auteri · M. Carini · D. Zagaglia · D. Montagnani · G. Gibertini · C.B. Merz · A. Zanotti

Received: date / Accepted: date

Abstract The purpose of this work is to develop an innovative procedure for reconstructing the pressure field from PIV velocity measurements of unsteady, incompressible flows. The proposed technique is based on a generalization of the Glowinski-Pironneau method for the uncoupled solution of the incompressible Navier–Stokes equations written in primitive variables and exploits a finite element discretization of the measurement grid. By virtue of the underlying mathematical formulation, the method is stable and more accurate than the other techniques proposed so far in the literature. The method is first applied to an exact solution of the Navier–Stokes equations, showing second order convergence of the L^∞ error for the pressure variable. The robustness of the method with respect to stochastic perturbations in the velocity field is then tested and the results compared with other techniques proposed in the literature. Finally, the proposed technique is applied to both phase-averaged and time-resolved PIV velocity measurements of the flow around a pitching airfoil employed to investigate the dynamic stall. The reconstructed pressure is compared with direct pressure measurements, showing very encouraging results.

Keywords Pressure field reconstruction · Particle Image Velocimetry (PIV) · Glowinski–Pironneau method

1 Introduction

The fast development of Particle Image Velocimetry (PIV) rapidly increased the interest in techniques able to estimate the aerodynamic loads on immersed bodies exploiting the measured velocity field, since the PIV measurement technique is able to provide the instantaneous flow field with sufficient accuracy. It must be said that Berton et al (2004) already computed the airloads on an helicopter blade using very accurate Laser Doppler velocity measurements, but this approach precludes to achieve an instantaneous field-measurement capability and the time needed to scan the area of interest with a sufficient resolution is usually unaffordable.

The possibility to compute the pressure field directly from PIV measurements is relevant for several reasons. Among these, the need to extract information on the pressure field over the whole domain, highlighting, for instance, strong vortical structures. Moreover, the possibility to obtain non-intrusive pressure measurements on an immersed body and the related airloads by direct

The present works are carried out in the GUM (Active Gurney on Main Rotor Blades) Research Project, being part of the Green Rotorcraft Integrated Technology Demonstrator of the Clean Sky programme, co-funded by the European Commission. The time-resolved PIV measurements were financed by the DLR project STELAR.

F. Auteri (✉) · M. Carini · D. Zagaglia · D. Montagnani · G. Gibertini · A. Zanotti
Dipartimento di Scienze e Tecnologie Aerospaziali, Politecnico di Milano
via La Masa 34, 20125 Milano, Italy Tel.: +39-02-23998046
E-mail: franco.auteri@polimi.it

C.B. Merz
German Aerospace Center (DLR),
Bunsenstrasse 10, 37073 Göttingen, Germany

integration. Eventually, but of the utmost importance, the interest in measuring the pressure field where a direct measurement is impossible, or impractical, such as for instance in regions far from the immersed body and on portions of the body surface where the pressure taps cannot be easily placed, such as on the trailing edge of an airfoil.

A thorough review of the history and state of the art of these methods can be found in the work by Van Oudheusden (2013). However, a quick overview of the available techniques highlighting their main features is presented here for reader's convenience. Since in this paper we are concerned with low Mach number flows, the incompressibility of the fluid will be assumed throughout.

In the past years, two different approaches have been proposed to compute the pressure field from PIV measurements. The first one is based on the solution of a Poisson equation for the pressure, obtained by taking the divergence of the momentum equation of the Navier–Stokes equations:

$$-\nabla^2 p = \rho \boldsymbol{\nabla} \cdot ((\boldsymbol{u} \cdot \boldsymbol{\nabla})\boldsymbol{u}) \,, \tag{1}$$

supplemented with Neumann boundary conditions obtained from the momentum equation, as proposed by Gurka et al (1999). The above formulation includes the simplification that the divergence of velocity is zero, as a consequence of the incompressibility assumption. In some cases, the Poisson equation has been supplemented by Dirichlet boundary conditions based on reliable pressure measurements (Violato et al, 2011) or, in other cases, on approximate, inconsistent[1] values obtained by heuristic assumptions about the physics of the problem. This technique mainly relies on the smearing properties of the Laplacian operator in order to smooth the experimental error on velocity. In any case, the solution depends significantly on the type of boundary conditions enforced, since, in the first case, the computation of the pressure gradient on the boundary amplifies significantly the experimental error or, in the last case, inconsistent boundary conditions are imposed.

The second technique, proposed by Baur and Köngeter (1999), consists in the spatial integration of the pressure gradient obtained from the momentum equation of the Navier–Stokes equations by means of finite differences:

$$\boldsymbol{\nabla} p = -\rho \left(\frac{\partial \boldsymbol{u}}{\partial t} + (\boldsymbol{u} \cdot \boldsymbol{\nabla})\boldsymbol{u} \right) + \mu \nabla^2 \boldsymbol{u}. \tag{2}$$

Unfortunately, this method suffers from error accumulation. It has been extended by Van Oudheusden et al (2007) to the compressible case, exploiting the gas law and the adiabatic flow condition instead of the continuity equation, since errors in the divergence computation due to three-dimensionality and to out-of-plane velocity gradients could accumulate. Liu and Katz (2006) computed the pressure field of a cavity using a Lagrangian approach in order to estimate the material derivative of the velocity field , instead of the separate computation of the time derivative and of the advection term. As shown at a later stage by Violato et al (2011), this approach is especially relevant in case of convection dominated flows (see also (De Kat and Van Oudheusden, 2012) and yields more accurate estimates of the pressure gradient when compared with the purely Eulerian one.

These techniques have been applied to several kinds of flow, e.g the flow past a square-section cylinder (De Kat and Van Oudheusden, 2012) or a circular cylinder with rotational oscillation (Fujisawa et al, 2005), the flow around a pair of bluff bodies in tandem configuration (Obi and Tokai, 2006), the turbulent boundary layer (Ghaemi et al, 2012). A truly challenging application of this method has been reported by Ragni et al (2012) who managed to compute the 3D pressure field around a propeller using stereoscopic PIV. Another application of these methods was the load estimation on a V-shaped body entering a quiescent fluid, see Panciroli and Porfiri (2013).

Further details about the above-mentioned techniques can be found in the review paper by Charonko et al (2010), where a detailed comparison of several methods for calculating the pressure field from 2D time-resolved velocity fields in incompressible flows is presented.

The innovative method proposed in this work aims at improving the accuracy of the previous methods by applying an innovative procedure to provide the Poisson equation for the pressure with accurate Dirichlet boundary conditions. Indeed, it is possible to obtain an uncoupled formulation of the incompressible Navier-Stokes problem, where the conditions that supplement the Poisson pressure problem, of an integral character (see Quartapelle (1993)), are derived exactly,

[1] Inconsistent means here that the error does not go to zero when the experimental error vanishes.

not depending on the type of flow considered. The Glowinski–Pironneau method can be used to obtain Dirichlet boundary conditions fully equivalent to such integral condition. Moreover, since the method involves the solution of a set of elliptic problems, it can provide a smoothing of the errors affecting the velocity measurements. While from a formal viewpoint the method is equivalent to the previous ones based on a Poisson equation for the pressure with Neumann boundary conditions computed starting from the momentum equation, the present method is more accurate when experimental errors are present and the solution of the Poisson equation is computed numerically. Indeed, the Poisson equation is numerically more stable with Dirichlet conditions than with Neumann conditions. Moreover, boundary conditions are obtained from pressure conditions of an integral character (Quartapelle and Napolitano, 1986) which can introduce a beneficial additional smoothing of the experimental error.

The present methodology can be applied to 2D, unsteady, incompressible flows either laminar or turbulent. In the present paper the methodology is introduced in Section 2, and assessed by both synthetic tests, in Section 3, and by applying it to both unsteady phase-averaged and time-resolved experimental datasets in Section 5.

2 Mathematical formulation and numerical discretization

2.1 Equations for incompressible flows

Let us consider the Navier–Stokes equations, supplemented by Dirichlet boundary conditions, in a control volume V with boundary $S = \partial V$:

$$\begin{cases} \dfrac{\partial \boldsymbol{U}}{\partial t} + (\boldsymbol{U}\cdot\boldsymbol{\nabla})\boldsymbol{U} - \nu\nabla^2\boldsymbol{U} + \boldsymbol{\nabla}P = \boldsymbol{F} & \text{in V,} \\ \boldsymbol{\nabla}\cdot\boldsymbol{U} = 0, & \\ \boldsymbol{U}\big|_S = \boldsymbol{B} & \text{on S,} \end{cases} \tag{3}$$

where $\boldsymbol{U}(\boldsymbol{x},t)$ represents the velocity vector field, $P(\boldsymbol{x},t)$ represents the pressure field divided by the fluid density and $\boldsymbol{F}$ represents a volume force divided by the fluid density. It is useful to note here that, in the particular application we are envisaging, $\boldsymbol{B} = \boldsymbol{B}(\boldsymbol{x},t^n)$ is the velocity measured on the boundary of the computational domain and therefore it is known, so that we can enforce full Dirichlet boundary conditions on the whole boundary ∂V. The more general case where the pressure is assigned on a portion of the domain has been discussed in the Appendix. If we are interested in the mean (phase-averaged) pressure field, one can introduce the corresponding version of the (Unsteady) Reynolds Averaged Navier–Stokes (U)RANS equations. For the sake of generality we will consider the URANS here. Since the velocity field is known only at discrete time intervals, we introduce the corresponding time discretization of the URANS equations:

$$\begin{cases} \dfrac{\boldsymbol{u}^n - \boldsymbol{u}^{n-1}}{\Delta t} + (\boldsymbol{u}^n\cdot\boldsymbol{\nabla})\boldsymbol{u}^n + \boldsymbol{\nabla}\cdot\langle\boldsymbol{u'}^n\otimes\boldsymbol{u'}^n\rangle - \nu\nabla^2\boldsymbol{u}^n = -\boldsymbol{\nabla}p^n + \boldsymbol{f}^n & \text{in V,} \\ \boldsymbol{\nabla}\cdot\boldsymbol{u}^n = 0, & \\ \boldsymbol{u}^n\big|_S = \boldsymbol{b}^n & \text{on S,} \end{cases} \tag{4}$$

where $\boldsymbol{u} = \langle\boldsymbol{U}\rangle$, $\boldsymbol{u'} = \boldsymbol{U} - \boldsymbol{u}$ and similarly for pressure. A backward-Euler discretization of the time derivative has been used in the formulation for the reader's convenience, but other schemes could be used as well. Since the only variable to be derived with respect to time is the velocity, and since the velocity field is known at every time instant from the PIV measurements, one can choose the best way to treat this term, namely to include it all in the right-hand side of equation (4) (explicit treatment) or to leave $\frac{\boldsymbol{u}^n}{\Delta t}$ on the left-hand side (implicit treatment). In this paper we will analyze both the implicit and explicit treatment of the time-derivative term.

Let us divide the momentum equation by the kinematic viscosity ν and denote the unknown fields at the new time level by $\boldsymbol{u} = \boldsymbol{u}^n$ and $p = p^n$, where now the letter p indicates the scaled

pressure $\nu^{-1}p \to p$. The problem can be rewritten as:

$$\begin{cases} (-\nabla^2 + \gamma\vartheta)\boldsymbol{u} + \boldsymbol{\nabla} p = \boldsymbol{g} & \text{in V,} \\ \boldsymbol{\nabla}\cdot\boldsymbol{u} = 0, & \\ \boldsymbol{u}\big|_S = \boldsymbol{b} & \text{on S,} \end{cases} \tag{5}$$

where $\gamma = \frac{1}{\nu\Delta t}$, $\boldsymbol{g} = \gamma(-(1-\vartheta)\boldsymbol{u}^n + \boldsymbol{u}^{n-1}) - \nu^{-1}[(\boldsymbol{u}^n\cdot\boldsymbol{\nabla})\boldsymbol{u}^n + \boldsymbol{\nabla}\cdot\langle\boldsymbol{u'}^n\otimes\boldsymbol{u'}^n\rangle - \boldsymbol{f}^n]$, which is an experimentally known quantity, and ϑ is an integer which determines the explicit (ϑ=0) or implicit ($\vartheta = 1$) treatment of the time-derivative term. The formulation of the steady-state problem can be obtained by simply setting $\gamma = 0$. With respect to the numerical solution of the Navier–Stokes equations, in the present case the pressure field is the only unknown. Nevertheless, by virtue of the existence and uniqueness of the solution of the above mathematical problem we are assured that, should the right hand side $\boldsymbol{g}$ and boundary datum $\boldsymbol{b}$ be computed starting from the "exact" velocity, then the exact solution of the above problem would give the exact pressure field but also the exact velocity field as a by product.

2.2 Uncoupling of the equations

Taking the divergence of the momentum equation (5) a Poisson equation for the pressure is obtained. Several approaches can be pursued to compute consistent conditions for the pressure, for instance the one adopted by Quartapelle and Napolitano (1986) relying on integral conditions for pressure. In the present work, the Glowinski–Pironneau decomposition has been adopted whose mathematical formulation reads:

$$\begin{cases} -\nabla^2 p = -\boldsymbol{\nabla}\cdot\boldsymbol{g} & & \\ (-\nabla^2 + \gamma\vartheta)\boldsymbol{v} = -\boldsymbol{\nabla} p + \boldsymbol{g}, & \boldsymbol{v}\big|_S = \boldsymbol{b} & \\ -\nabla^2\varphi = \boldsymbol{\nabla}\cdot\boldsymbol{v}, & \varphi\big|_S = 0, & \frac{\partial\varphi}{\partial n}\big|_S = 0. \end{cases} \tag{6}$$

In the above system, beside the Poisson equation for the pressure and the Helmholtz equation for the auxiliary variable $\boldsymbol{v}$ which takes the place of the velocity field, a Poisson equation for the auxiliary variable φ is added to enforce the solenoidality condition. In fact, as it can be noticed from system (6), the equation for φ is supplemented by overabundant boundary conditions, which are necessary to enforce the incompressibility constraint all over the domain as shown by Glowinski and Pironneau (1979), while the Poisson equation for pressure lacks boundary conditions, implying that the system is still coupled through the boundary conditions. This means that no boundary conditions are required for the pressure which plays the role of a Lagrange multiplier to enforce the incompressibility constraint on the velocity field, in this case represented by the auxiliary vector field $\boldsymbol{v}$.

Let us introduce the following decomposition of the unknowns:

$$\begin{Bmatrix} p(\boldsymbol{x}) \\ \boldsymbol{v}(\boldsymbol{x}) \\ \varphi(\boldsymbol{x}) \end{Bmatrix} = \begin{Bmatrix} p^0(\boldsymbol{x}) \\ \boldsymbol{v}^0(\boldsymbol{x}) \\ \varphi^0(\boldsymbol{x}) \end{Bmatrix} + \sum_{k=1}^{\infty} \begin{Bmatrix} p^k(\boldsymbol{x}) \\ \boldsymbol{v}^k(\boldsymbol{x}) \\ \varphi^k(\boldsymbol{x}) \end{Bmatrix} \lambda^k. \tag{7}$$

By virtue of its linearity, the original problem (6) can be split in the following sets of equations:

$$\begin{cases} -\nabla^2 p^0 = -\boldsymbol{\nabla}\cdot\boldsymbol{g}, & p^0|_S = 0 \\ (-\nabla^2 + \gamma\vartheta)\boldsymbol{v}^0 = -\boldsymbol{\nabla} p^0 + \boldsymbol{g}, & \boldsymbol{v}^0|_S = \boldsymbol{b} \\ -\nabla^2\varphi^0 = \boldsymbol{\nabla}\cdot\boldsymbol{v}^0, & \varphi^0|_S = 0, \end{cases} \tag{8}$$

$$\begin{cases} -\nabla^2 p^k = 0, & p^k|_S = \mu^k & \\ (-\nabla^2 + \gamma\vartheta)\boldsymbol{v}^k = -\boldsymbol{\nabla} p^k, & \boldsymbol{v}^k|_S = 0 & k = 1:\infty \\ -\nabla^2\varphi^k = \boldsymbol{\nabla}\cdot\boldsymbol{v}^k, & \varphi^k|_S = 0, & \end{cases} \tag{9}$$

where μ^k is the k-th basis function of the space of trace functions, namely the space of functions defined on the domain boundary. In this case, the Lagrangian finite-element basis functions, which

are 1 in one point of the boundary grid and 0 on the remaining points, has been selected. To obtain the discretized problems, the space of the trace functions is truncated to a finite dimension N_D equal to the number of boundary degrees of freedom (d.o.f.), and the μ^k functions are replaced by the trace of the discrete FEM basis functions that do no vanish on the whole boundary. It is therefore necessary to compute the solution of the first system and compute as many solutions for the k problems as the number of d.o.f.s on the boundary, each time with a different boundary condition for p^k. As we can appreciate, the PIV data only appear in system (8), whereas the k problems (9) are independent from the velocity data, hence they depend on the grid shape only. To reconstruct the pressure field, one has to compute also λ^k, the coefficients of the expansions which represent, with the above choice of the trace functions, the pressure values on the boundary nodes. To do so, one can use the overabundant Neumann boundary condition for φ. By inserting the expansion for φ in $\frac{\partial \varphi}{\partial n} = 0$ and recasting the problem in variational formulation, one obtains

$$\oint_S w \frac{\partial \varphi^0}{\partial n} + \sum_{k=1}^{N_D} \oint_S w \frac{\partial \varphi^k}{\partial n} \lambda^k = 0, \tag{10}$$

where w is an arbitrary test function which can be assumed different from zero only in a narrow shell along the boundary, so that the volume integrals above can be evaluated efficiently. Exploiting the divergence theorem and the Poisson equation for φ^0 and φ^k, one obtains the following system of equations:

$$\sum_{k=1}^{N_D} \int_V (w \boldsymbol{\nabla} \cdot \boldsymbol{v}^k - \boldsymbol{\nabla} w \cdot \boldsymbol{\nabla} \varphi^k) \lambda^k = - \int_V (w \boldsymbol{\nabla} \cdot \boldsymbol{v}^0 - \boldsymbol{\nabla} w \cdot \boldsymbol{\nabla} \varphi^0) \tag{11}$$

that, once discretized, will lead to a linear system whose solution is a vector containing λ_k. Once the coefficients of the expansion have been computed, the pressure field can be reconstructed:

$$p(\boldsymbol{x}) = p^0(\boldsymbol{x}) + \sum_{k=1}^{N_D} p^k(\boldsymbol{x}) \lambda^k. \tag{12}$$

It should be noticed that p does not exactly correspond to the physical pressure field, since the equations have been scaled by the kinematic viscosity and density. The physical pressure values are obtained by multiplying the computed pressure field by ν and ρ and adding a constant pressure value to match the measured pressure in an arbitrary point of the flow field. This last step cannot be avoided by any technique exploiting the incompressible Navier–Stokes equations to compute the pressure. In fact in these equations, the pressure field is determined up to an additive constant when full Dirichlet boundary condition for the velocity variable are enforced. This problem is not a significant limitation, since one is generally interested in pressure differences rather than absolute pressure values.

2.3 Numerical discretization

Once the problems (8) and (9) have been recast in variational form, they can be discretized. The Finite Element Method (FEM) has been chosen by virtue of its efficiency, accuracy and geometric flexibility and since it allows one to directly translate the weak formulation in the discrete algebraic equations. Let $\mathcal{T}_h$ be a regular triangulation of the domain V, built so that the nodes correspond to the centre of every PIV interrogation window. For this problem we will choose a linear piecewise approximation for p and φ and a quadratic piecewise approximation for $\boldsymbol{u}$, namely we select the vector spaces X_h^1 and X_h^2 respectively built on the grid $\mathcal{T}_h$. The choice of two different vector spaces is necessary to satisfy the LBB condition, which must be satisfied even if the pressure and velocity equations are uncoupled, see Guermond and Quartapelle (1998). Introducing the basis ϕ_j, $1 \leq j \leq N$ for the vector space X_h^1 and the basis ψ_j, $1 \leq j \leq M$ for the vector space X_h^2, we can

now express the approximate solutions by means of these bases:

$$\begin{cases} p_h(\boldsymbol{x}) = \sum_{j=1}^{N} \phi_j(\boldsymbol{x}) p_j, & p_h(\boldsymbol{x}) \in X_h^1 \\ v_{l_h}(\boldsymbol{x}) = \sum_{j=1}^{M} \psi_j(\boldsymbol{x}) v_{l_j}, & v_{l_h}(\boldsymbol{x}) \in X_h^2, \quad l = 1 : n_D \\ \varphi_h(\boldsymbol{x}) = \sum_{j=1}^{N} \phi_j(\boldsymbol{x}) \varphi_j, & \varphi_h(\boldsymbol{x}) \in X_h^1, \end{cases} \tag{13}$$

where N and M are the number of $\mathbb{P}^1$ and $\mathbb{P}^2$ nodes, respectively, and n_D is the number of space dimensions. By substituting these expressions in the weak formulations, one obtains a set of algebraic sparse linear systems whose solution represents the nodal values of the unknowns.

Since the FEM discretization of the Poisson and Helmholtz problems, equations (8) and (9), is very well known, see for instance Aziz and Werschulz (1980), let us focus on the discretization of the integral equation (11). By considering the i-th basis function w^i of the trace space, corresponding to the i-th Dirichlet boundary node, we have:

$$\sum_{k=1}^{N_D} \int_V (w^i \boldsymbol{\nabla} \cdot \boldsymbol{v}^k - \boldsymbol{\nabla} w^i \cdot \boldsymbol{\nabla} \varphi^k) \lambda^k = - \int_V (w^i \boldsymbol{\nabla} \cdot \boldsymbol{v}^0 - \boldsymbol{\nabla} w^i \cdot \boldsymbol{\nabla} \varphi^0) \qquad i = 1 : N_D. \tag{14}$$

Equation (14) represents the i-th row of the linear system $A\lambda = \mathbf{a}$, where:

$$A_{ik} = \int_V (w^i \boldsymbol{\nabla} \cdot \boldsymbol{v}^k - \boldsymbol{\nabla} w^i \cdot \boldsymbol{\nabla} \varphi^k), \tag{15}$$

$$a_i = - \int_V (w^i \boldsymbol{\nabla} \cdot \boldsymbol{v}^0 - \boldsymbol{\nabla} w^i \cdot \boldsymbol{\nabla} \varphi^0). \tag{16}$$

The k-th column of matrix A can be computed once the k-th problem (9) has been solved, whereas the computation of the right-hand side requires the solution of system (8). The influence matrix A is positive semi-definite. Because of full Dirichlet boundary conditions imposed on the velocity field, the pressure is determined up to an additive arbitrary constant. This singularity can be eliminated by imposing either a prescribed mean value or the pressure value in one node. This can be achieved in several ways, the easiest one consisting of simply replacing the row corresponding to the node where we want to impose the pressure value with a row of zeros, but for the diagonal term which is set to one. The corresponding term on the right-hand side is set equal to the pressure value to be imposed. This method is definitely of simple implementation, however it can be seen that the modified matrix A, especially for low Δt and ν, is extremely ill-conditioned, and therefore a considerable error is introduced in its solution. In order to avoid this problem, the solution can be computed through the diagonalization of matrix A, which is computationally onerous but affordable, since it has to be computed only once.

3 Validation and Error analysis

3.1 Convergence analysis

The whole method has been tried on a test-case with a known solution to investigate its accuracy and convergence properties. The following divergence-free velocity vector field and pressure field are considered:

$$\begin{aligned} &\boldsymbol{u}_{\mathrm{ex}}(\boldsymbol{x},t) = \tilde{\boldsymbol{u}}(\boldsymbol{x}) q(t), \\ &\tilde{u}_x(\boldsymbol{x}) = -\cos x \sin y, \\ &\tilde{u}_y(\boldsymbol{x}) = \sin x \cos y, \\ &q(t) = \sin(2\pi t), \\ &p_{\mathrm{ex}}(\boldsymbol{x},t) = -\frac{1}{4}[\cos(2x) + cos(2y)] q^2(t), \end{aligned} \tag{17}$$

which is the exact solution $(\boldsymbol{u},p)$ in $V \subset \mathbb{R}^2 : [-1,1]^2$ to the unsteady Navier–Stokes equations, with the following choice of the volume force: $\boldsymbol{f}(\boldsymbol{x},t) = \tilde{\boldsymbol{u}}(\boldsymbol{x})[q'(t) + 2\nu q(t)]$. For the convergence analysis we consider the normalized L^∞ norm (maximum norm) of the error between the exact

and the reconstructed solution, defined as:

$$\mathrm{Err}_\infty = \frac{\|p - p_{\mathrm{ex}}\|_\infty}{\|p_{\mathrm{ex}}\|_\infty} = \frac{\max\limits_{\boldsymbol{x}\in\Omega}|p - p_{\mathrm{ex}}|}{\max\limits_{\boldsymbol{x}\in\Omega}|p_{\mathrm{ex}}|}. \tag{18}$$

The L^∞ norm has been chosen since it provides pieces of information more suitable to analyse the accuracy of the method from the viewpoint of the experimentalist. The error, computed for several values of the grid spacing h, is represented in the logarithmic-scale plot of Figure 1. The analysis has been carried out for two different values of the time interval Δt, and for both the explicit and the implicit treatment of the time derivative, with $\nu = 10^{-5}\ m^2/s$ and $\bar{t} = 1/8\ s$.

As it can be appreciated from the figure, this method provides a second order spatial convergence for the reconstructed pressure for both the explicit and the implicit treatment of the time derivative. Some discrepancies can be observed, for small h, with the largest value of Δt adopted. This behaviour can be explained by the fact that for small h, the error due to the time discretization becomes of the same order of magnitude and eventually bigger than the spatial one, implying the saturation of the convergence curve for small h.

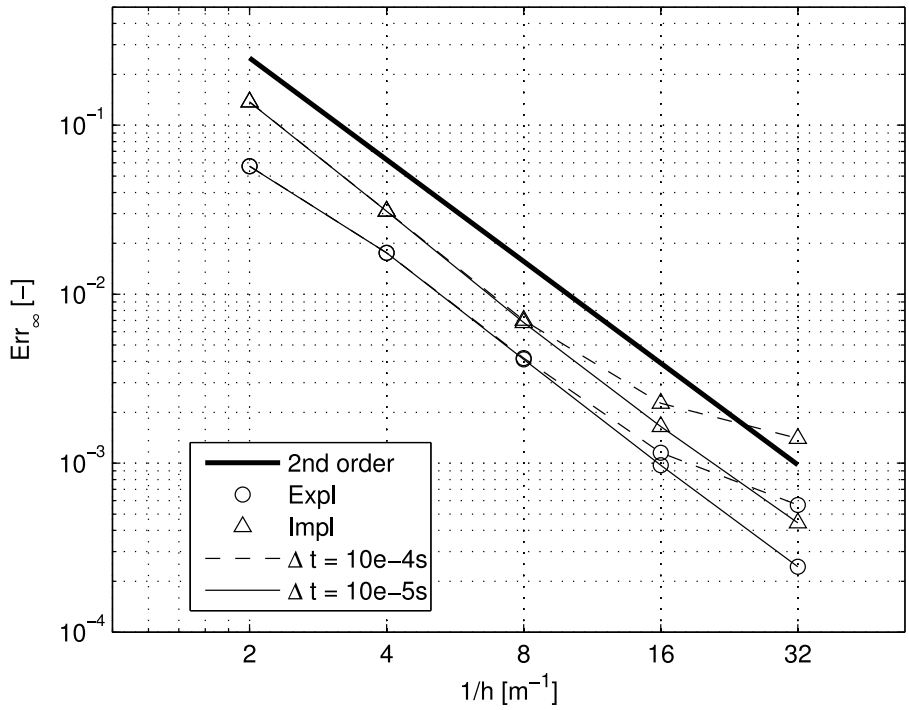

Fig. 1: Convergence analysis for the reconstructed pressure. Results for different treatments of the time derivative and Δt

3.2 Stochastic error analysis

To test the robustness of the method when measurement errors on velocity are present, a Monte Carlo simulation on a slightly modified test case (with respect to the one described in section 3.1) has been conducted. The only parameter that has been changed is the function of time $g(t) = 1 - \exp(-4t)$ and the time instant considered, $\bar{t} = 1\ s$. The simulation has been carried out with the following methodology:

1. Both the velocity fields at the current and previous time instants are perturbed with a stochastic error. The error has a Gaussian distribution with null expected value, hence we assume an ideally calibrated instrument, and standard deviation $\sigma_{pert} = \frac{0.01}{2\sqrt{3}} \simeq 3 \cdot 10^{-3}\ m/s$, generated using the method developed by Box and Muller (1958). The perturbation is uncorrelated between the two velocity components and in the spatial domain. The same perturbation has been applied to the two time steps, since an uncorrelated velocity perturbation in time would be amplified too much, especially for small Δt. Therefore, the perturbation corresponds to a white noise in space.
2. The proposed method is applied to the perturbed velocity field, with the following choice of the parameters: $\nu = 10^{-5}\ m^2/s$, $\Delta t = 10^{-3}\ s$, $h = 0.05\ m$.
3. The procedure is repeated an adequate amount of times, each time with a different stochastic perturbation, which must satisfy the statistical properties just introduced. The computed pressure errors are stored for each realization of the Monte Carlo simulation.
4. The produced database is then post-processed to compute the statistical properties of the pressure error.

3.2.1 Preliminary analysis

A preliminary analysis with a reduced amount of simulations is carried out to check the robustness of the method for both the explicit ($\vartheta = 0$) and implicit ($\vartheta = 1$) treatment of the time derivative. The average pressure error, computed in L^∞ norm and normalized by the L^∞ norm of the exact solution, is shown in Table 1.

-	Pressure error
Implicit	2.81
Explicit	1.33 E-002

Table 1: Preliminary stochastic analysis: L^∞ norm of the pressure error for the explicit ($\vartheta = 0$) and implicit ($\vartheta = 1$) treatment of the time derivative.

As it can be seen from the table, the implicit method presents an unacceptable error in the pressure computation. This is caused by the fact that for small Δt and ν, hence great γ, the laplacian term of the Helmholtz equation for $\boldsymbol{u}$ is everywhere negligible with respect to the reaction term but for a thin layer near the boundary, leading to a singular perturbation problem. This fact generates oscillations in the velocity fields when discretized by the Bubnov–Galerkin method. If the boundary value of velocity is affected by an error, this will turn in its great amplification when the pressure is computed. The same problem is not present in the explicit method since the velocity has to satisfy a Poisson equation.

3.2.2 Detailed analysis

A more accurate Monte Carlo analysis has been carried out, based on a set of 1000 realizations, which are sufficient to reach the convergence of the standard deviation of the perturbation up to the second significant figure. The flow and discretisation parameters are the same as for the preliminary analysis, and an explicit treatment of the time derivative has been adopted since it guarantees a better robustness to velocity measurement errors.

At the end of each simulation, the local normalized pressure error, defined as follows:

$$\mathrm{Err} = \frac{p - p_{ex}}{\|p_{ex}\|_\infty} \tag{19}$$

is stored for every grid node. At the end of the whole Monte Carlo Simulation, the average and the standard deviation σ of Err is computed for each grid node. The results are presented in Figure 2.

Let us first analyse the space distribution of the mean value of the error. As it can be appreciated from figure 2a, the mean value of the pressure error is globally quite small, and follows the profile of

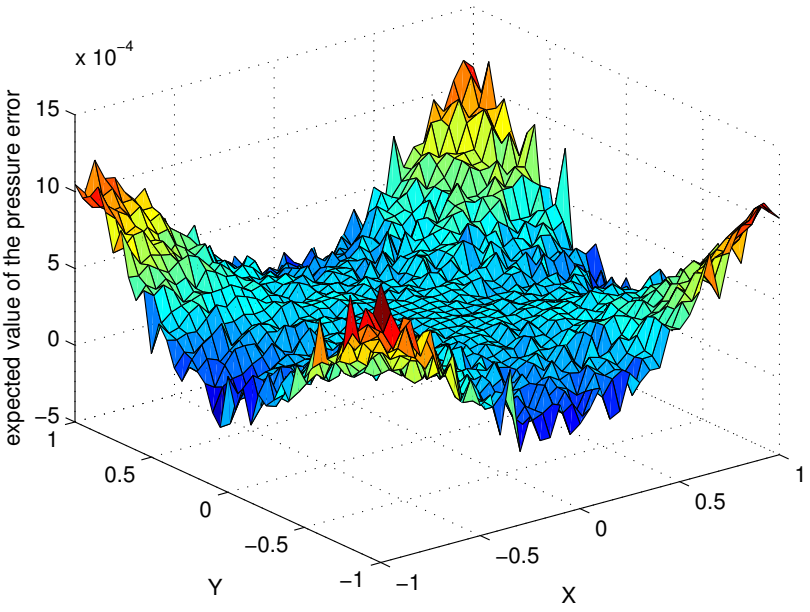

(a) *Mean Value of the local pressure error*

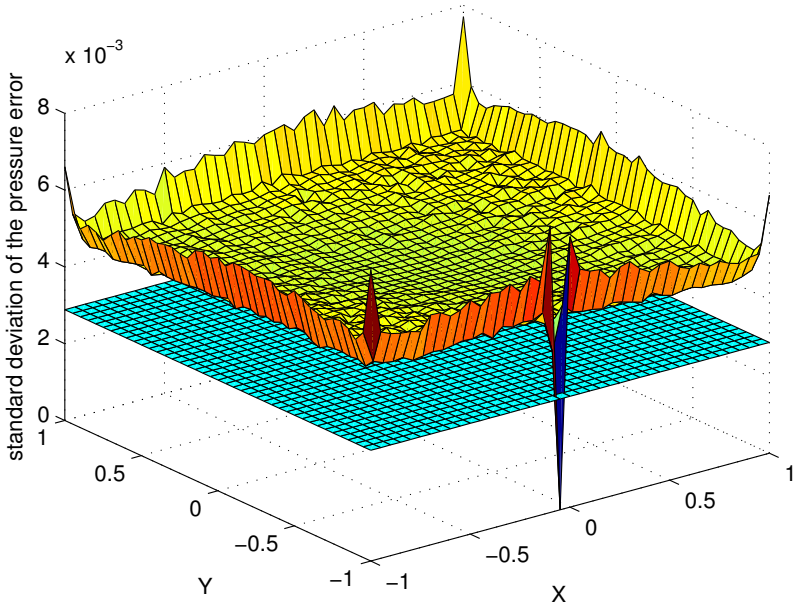

(b) *Standard deviation of the local pressure error*

Fig. 2: Test case with prescribed stochastic perturbation of the velocity field: expected value (a) and standard deviation (b) of the pressure error

the discretization error. This means that locally the mean value of the error due to the perturbation is approximately zero, which was expected since the perturbation has zero mean value. In usual applications, where the exact solution is not available, an a posteriori estimator could be used to obtain an estimate of the numerical error.

A more interesting piece of information can be deduced from the plot of the standard deviation of the error, Figure 2b. Here the plane represents the standard deviation of the perturbation. As it can be seen, the standard deviation of the perturbation is amplified homogeneously on the inner nodes, with a ratio $\sigma/\sigma_{pert} \simeq 1.6$. The same phenomenon can be appreciated among the nodes belonging to the boundary, but here the ratio σ/σ_{pert} grows to approximately 2. This analysis shows that the most sensitive part for the amplification of the error standard deviation is the border of the domain, which is generally where we are more interested in knowing the pressure value (e.g. to compute the loads), fortunately the amplification of the perturbation is rather small, since the error on the reconstructed pressure is just twice the perturbation.

The null value that can be observed on the boundary of the domain in Figure 2b can be explained by the fact that, since pressure is defined up to an additive constant, the exact value of the pressure has been imposed in that point and therefore the error is always equal to zero in that point, and its variance too.

The very same Monte Carlo analysis has been repeated with different values of σ_{pert}. The results are reported in Table 2:

σ_{pert}	$\sigma_{center}/\sigma_{pert}$	$\sigma_{border}/\sigma_{pert}$
0.001	1.54	1.98
0.010	1.54	1.98
0.030	1.60	2.02

Table 2: Stochastic analysis for different values of the standard deviation of the perturbation

As it can be appreciated, the ratio between the error standard deviation and σ_{pert} is almost independent from the standard deviation of the perturbation, which is a typical behaviour of linear problems.

3.3 Comparison with other techniques

The proposed method, in its explicit form, is here compared with other similar techniques in terms of robustness to the velocity error. The same approach of Charonko et al (2010) has been pursued. An exact solution of the incompressible Navier–Stokes equations has been considered, the decaying Taylor vortex. The corresponding velocity field has been perturbed by a zero-mean error with Gaussian distribution of prescribed standard deviation. The considered tangential component of the velocity field and the pressure field are:

$$V_\theta(r,t) = \frac{H}{8\pi}\frac{r}{\nu t^2}\exp\left(-\frac{r^2}{4\nu t}\right) \tag{20}$$

$$P_{ex}(r,t) = -\frac{\rho H^2}{64\pi^2\nu t^3}\exp\left(-\frac{r^2}{2\nu t}\right) + P_\infty, \tag{21}$$

where H is a measure of the angular momentum in the vortex, r is the distance from the origin and P_∞ is the pressure at an infinite distance from the origin, here set to zero. The employed grid, the time step and the problem parameters were set equal to those used by Charonko et al (2010). The exact velocity field is perturbed with a Gaussian error defined as a percentage of the local value of the velocity. The same 26 time instants of the cited article are considered. Let us denote by δ_{kl} the normalized pressure error at node k at time instant l, computed as the difference between the computed pressure value and the exact solution divided by the pressure drop at that time instant,

namely $P_{ex}(0,t)$, as in (19). The global indicator considered for the pressure error is the following:

$$\sigma_{\text{tot}} = \sqrt{\frac{1}{LK}\sum_{k=1}^{K}\sum_{l=1}^{L}\left(\delta_{kl} - \bar{\delta}_l\right)^2}, \tag{22}$$

where $\bar{\delta}_l$ is the average value of δ_{kl} at the time instant l, K is the total number of nodes and L is the total number of time instants considered. The results in terms of σ_{tot} are presented in table 3 for two different values of the velocity error (1%, 10%). Moreover, two different time-discretization schemes were tested: the first order backward-Euler scheme (BDF) presented in equation (4) and a second-order central-difference scheme (CDF) in which the time derivative is approximated as $\frac{\boldsymbol{u}^{n+1}-\boldsymbol{u}^{n-1}}{2\Delta t}$. Results are compared in Table 3 with those obtained by Charonko et al. for the two most accurate techniques, namely:

Method A Poisson problem for pressure in conservative formulation (i.e. with the convective term written in the form $\rho\boldsymbol{\nabla}\cdot(\boldsymbol{u}\otimes\boldsymbol{u})$) with full Neumann boundary conditions, implemented by means of second-order finite differences.

Method B Standard line integration of the pressure gradient by means of second-order finite differences. In order to minimize the effect of the choice of starting location and integration path on the final results, the result was computed for all eight possible combinations of corner and integration direction, and the resulting fields averaged.

Velocity perturbation	σ_{tot} Proposed method, BDF	σ_{tot} Proposed method, CDF	A	B
1%	3.32%	1.36%	5%	12%
10%	36.52%	21.38%	53%	87%

Table 3: Stochastic analysis: comparison of the total RMS of the pressure error obtained by the present method (σ_{tot}) with the one obtained by other techniques (Charonko et al, 2010). Method A is Poisson conservative, while method B is line integration.

As it can be appreciated, an excellent propagation of the velocity error can be obtained by means of the proposed technique, better than the one obtainable by the other methods developed so far. As expected, the second order central difference formula (CDF) approach yields more accurate results, since it introduces a further smoothing of the velocity error. A 1.36% standard deviation on pressure is obtained starting from a 1% standard deviation of the velocity perturbation, which is quite remarkable.

These results were obtained by applying an uncorrelated error between the two time steps. The same test was repeated applying the same perturbation to both time steps, revealing a 0.07% pressure error against a 1% perturbation. This confirms the fact that the most important contribution to the pressure error arises from the time discretization rather than from the spatial one. The problem is further accentuated for quite small Δt, revealing an issue if such techniques are adopted for time-resolved PIV. For this reason the central difference approach is recommended for such applications.

Differently from the results obtained in section 3.2.2, the linear behaviour of the pressure error with respect to the velocity one cannot be recognized any more. This is due to the fact that σ_{tot} is a global parameter that resumes the behavior of the method at different time instants, hence representing different problems. By repeating the same procedure at only one time instant, the linearity of the pressure error with respect to the velocity one is recovered.

3.4 Robustness to out-of-plane velocity components

In order to test the robustness of the method when out-of-plane velocity components are present, the very same procedure of section 3.3, with the time derivative computed with backward differ-

ences, has been applied to the decaying Taylor vortex after its axis has been rotated by an angle θ around the $y-$axis, leading to a systematic bias in the resolved in-plane measurements that violates the incompressibility constraint. This could also simulate a misalignment of the PIV laser sheet with respect to the flow plane. Results in terms of $\sigma_{\rm tot}$ are presented in Table 4 for different values of θ.

θ	$\bar{\delta}$	$\sigma_{\rm tot}$
0 deg.	0.01 %	3.32 %
5 deg.	0.02 %	3.32 %
15 deg.	0.08 %	3.31 %
30 deg.	15.31 %	21.50 %

Table 4: Mean value and standard deviation of the pressure error as a function of the vortex tilting angle

It can be noticed that the method preserves its overall performance for relatively large vortex tilting angles, and that the performance starts to decrease at 30 degrees. A similar behaviour is observed also by Charonko et al (2010) for the other techniques.

4 Test rig and experimental setup

4.1 Test rig and experimental setup for the phase-averaged measurements

4.1.1 Test rig

The experimental campaign to acquire the phase-averaged PIV database was carried out at Politecnico di Milano, taking advantage of the low-speed, closed-return wind tunnel at the Department of Aerospace Science and Technology. This wind tunnel has a rectangular test section, 1.5 m high and 1 m wide, and can achieve a maximum wind speed of 55 m/s, with a turbulence level lower than 0.1%.

The blade section model that was employed for the experimental campaign had been already employed in several experimental investigations about the dynamic stall process and perpendicular blade vortex interaction, for further details see Zanotti and Gibertini (2012) and Gibertini et al (2013). The chosen airfoil is a NACA 23012.The chord of the blade section model is 0.3 m and the aspect ratio is 3.1. The model is composed by three aluminium machined external sections connected to an internal metallic frame also made of aluminium. The model central section is interchangeable depending on the measurement technique involved. In particular, one central section is equipped with 21 pressure taps positioned along the midspan airfoil contour. A different central section without taps is used to perform PIV surveys in the model midspan plane. The blade section model is mounted horizontally in the wind tunnel test section and is hinged about the quarter-chord axis on two external, tubular steel shafts positioned on self-aligning bearings, as depicted in Figure 3. The model is installed on a heavy metallic supporting structure composed by steel beams and aluminium profiles.

The oscillating-airfoil motion around the axis at 25% of the chord is driven by a brushless servomotor through a 12:1 gearbox drive.The model pitching motion is controlled by a proportional-derivative action using an interface software purposely developed in Labview. Two encoders are mounted directly on the outer shaft: the first one is a 2048 imp/rev absolute digital encoder, used for the feedback control, whereas the second one is a 4096 imp/rev incremental analog encoder, used to determine the current model position. More details about the description of the pitching airfoil experimental rig can be found in Zanotti (2012).

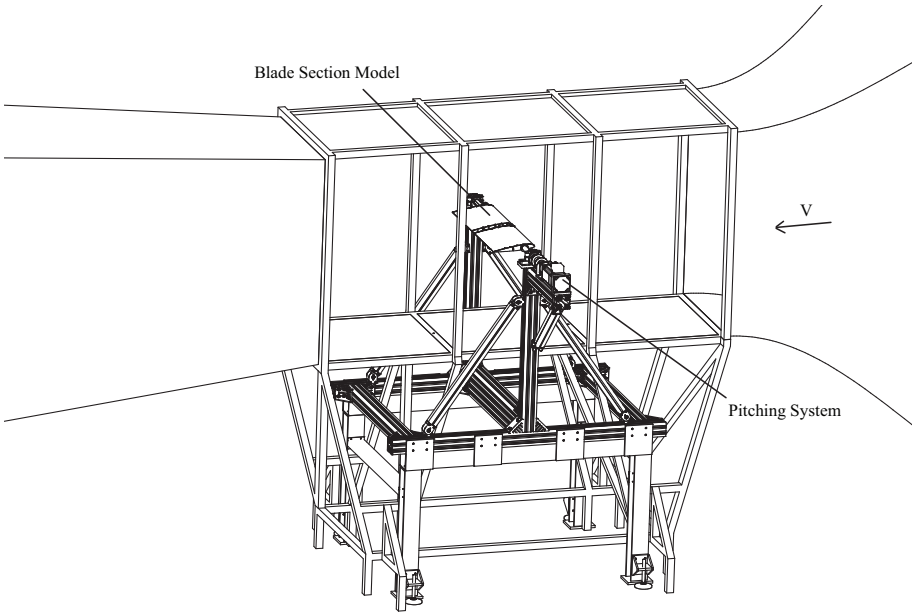

Fig. 3: Test rig

4.1.2 Experimental Setup

The experimental campaign employed both PIV and unsteady pressure measurements since the goal of the activity is a comparison between the reconstructed and measured pressure fields.

The midspan section of the model is equipped with 21 Kulite XCS-093 pressure transducers that are slightly more concentrated near the leading edge. The pressure tap positions are shown in Figure 4. The pressure tap numbering starts from the leading edge and follows a closed loop from the upper to the lower surface.

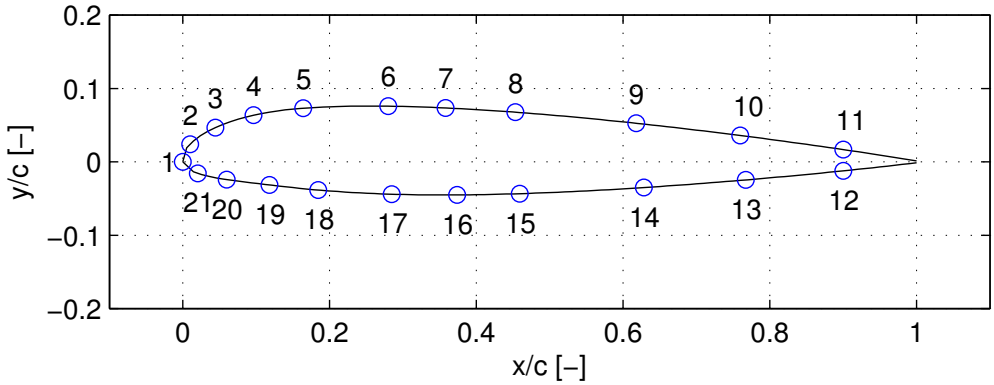

Fig. 4: Position of the pressure taps on the NACA 23012 model midspan section

The pressure signals have been acquired using a National Instruments compact data acquisition system cDAQ-9172 equipped with six NI 9237, 24 bit sampling bridge modules. The transducer signals have been acquired with a 50 kHz simultaneous sampling rate on 21 channels for a time period corresponding to 30 complete pitching cycles. The model angular position has been measured by the incremental encoder simultaneously with the pressure transducer signals. The simultaneous acquisition of the encoder signal has been used to evaluate the phase averaged pressures on the airfoil surface.

The PIV system is composed of a Litron NANO-L-200-15 Nd:Yag double pulsed laser with 200 mJ output energy and a wavelength of 532 nm and an Imperx ICL-B1921M CCD camera with a 12 bit, 1952 $\times$ 1112 pixel array. The laser was positioned on the top of the wind tunnel test section while the camera is positioned on one side of the test section. The camera was equipped with a Nikkor 50 mm lens. The synchronization of the laser pulses with the camera exposure was controlled by a 6 channel Quantum Composer QC9618 pulse generator. The digital encoder signal mounted on the oscillating model triggered every 1/rev the laser and the camera at the angle of attack of the oscillating model required for the test. The digital images were captured using a GigaEthernet EBus connection. A particle generator PIVpart30 by PIVTEC with Laskin atomizer nozzles was used for the seeding, consisting in small oil droplets with diameter in the range of 1-2 μm.

For every flow condition, two different PIV measurement windows (152 mm $\times$ 86 mm) have been considered at the midspan of the employed wing section model: the first one positioned near the upper surface of the leading edge (fin1) and the second one positioned near the upper surface of the trailing edge (fin2). The two measurement windows are represented in Figure 5:

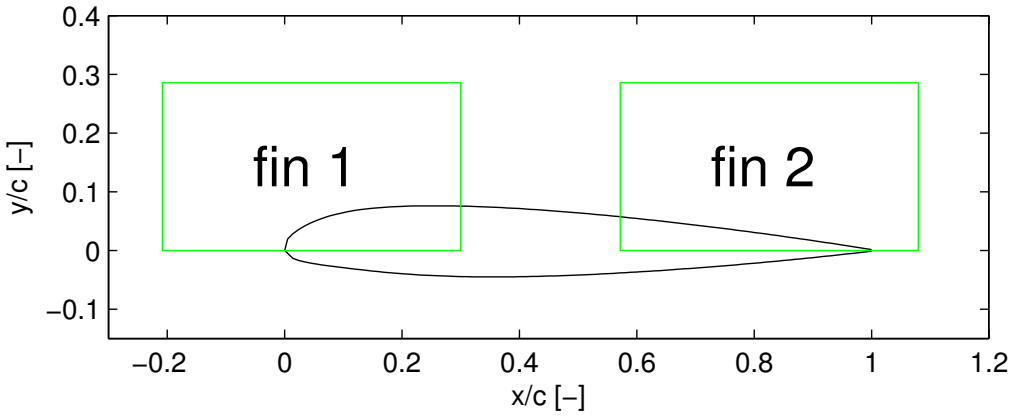

Fig. 5: Position of the PIV measurement windows with respect to the blade section

The image post-processing has been carried out by means of the PIVview 2C/3C software, which implements a multi-grid algorithm, starting from 96 $\times$ 96 pixel interrogation windows up to 32 $\times$ 32, with an overlap factor of 50 %.

All the experiments were carried out with a wind speed of approximately 30 m/s, a Reynolds number $Re = \frac{U_\infty c}{\nu}$ of approximately $6 \cdot 10^5$, where c is the airfoil chord, a Mach number of approximately 0.09 and a reduced frequency $k = \frac{\Omega c}{2U_\infty}$ of 0.1 ($f = \Omega/2\pi = 3.2$ Hz).

Steady surveys have been conducted by clamping the model shaft. Then, to test the proposed method on a challenging unsteady flow, a moving, pitching airfoil in dynamic stall conditions has been considered. The prescribed time history of the angle of attack for the oscillating airfoil is

$$\alpha(t) = \alpha_0 + A\sin(\Omega t). \tag{23}$$

For each measurement window, 1000 velocity fields have been sampled and post-processed to compute the average field and the Reynolds-stress tensor. When we are interested in an unsteady computation of the pressure field a set of velocity fields have to be acquired, for every configuration, at different times before and after the considered instant, depending on which time-integration scheme is adopted.

4.2 Test rig and experimental setup for the time-resolved measurements

To investigate the accuracy of the proposed technique when applied to time-resolved PIV datasets, further experiments, where simultaneous time-resolved PIV and pressure measurements

have been acquired, were carried out at DLR in the low-speed closed-circuit wind tunnel DLR-SWG, with a test section of 2.4 m × 1.6 m (width × height). The measurements were performed over the suction side of a sidewall-mounted finite wing with a chord length of 0.27 m, an aspect ratio of six and a positive linear twist of 5.5°. The finite wing used the DSA-9A helicopter-main-rotor airfoil. The free-stream velocity was set to 55 m/s resulting in a chord based Reynolds number of $9 \cdot 10^5$ and a Mach number of 0.16. The model was pitched sinusoidally about the quarter chord axis at $\alpha = 9° \pm 6°$ at the wing root, with a frequency of 3.2 Hz ($k = 0.05$). The sinusoidal motion was driven by a Parker 190ST6M motor with a $4:1$ gearbox. The motor controller features a cascaded control for current, rotational speed and position. An additional iterative learning control for the position input was developed to achieve a high repeatability of the motion.

To limit the influence of the wing tip, the measurements were carried out in a plane aligned with the free stream and 0.52 m (1.93c) inboard of the tip. The model was equipped with 22 Kulite XCQ-093 unsteady-pressure transducers at that spanwise position, 15 of which were located on the suction side of the airfoil. The flow was seeded with 1 μm Di-Ethyl-Hexyl-Sebacat (DEHS) droplets and illuminated with a Litron LDY304 dual cavity laser. Particle images were acquired with two PCO.dimax cameras at a resolution of 1680 × 1472 pixels and an acquisition rate of 1 kHz per image pair in a stereoscopic configuration. The PIV evaluation was performed with the commercial software Davis 8 (LaVision) using a multi-grid scheme with two final passes. The final interrogation window size was 32×32 pixels with an overlap of 50%, resulting in a grid spacing of 3.6 mm (1.3%c). Assuming a precision of 0.1 pixels for the determined displacement, the uncertainty in the velocity is approximately 3% of U_∞. The timing of the pressure data and the PIV recordings was synchronised by means of a camera feedback signal and a fast photodiode.

5 Results

5.1 Phase-averaged database

In this section, we present the results obtained by using the proposed method to reconstruct the pressure field around the NACA 23012 airfoil from PIV measurements of the related velocity field. Herein the method is applied without any modification of the jagged grid inherited from the PIV data postprocessing, i.e. the grid which is obtained by simply dropping the points which lie outside the flow field. The following two test cases have been analysed:

1. fixed airfoil with $\alpha = 9°$
2. oscillating airfoil with $\alpha_0 = 10°$, $A = 10°$ and $\alpha = 10°$ downstroke

To deal with the Reynolds averaged Navier-Stokes equations, both the mean field and the Reynolds stress tensor components have been computed by phase–averaging over 1000 samples of the velocity field for each selected phase. This high number of samples allows to smooth out the high frequency errors and therefore to reduce the error associated with the time derivative term in the Navier–Stokes equations, which otherwise could be quite severe. In order to compare the obtained numerical results with the available measures gathered from Kulite transducers on the airfoil surface, the arbitrary offset of the computed pressure field must be fixed. In Case 1 this was accomplished by applying the Bernoulli theorem in an arbitrary point far from the airfoil surface, while in Case 2 the offset was fixed by imposing the pressure equal to the measured one in a node near the pressure taps, since the steady version of the Bernoulli theorem cannot be employed anymore.

The input velocity fields (magnitude and streamlines), the reconstructed pressure coefficient fields and the comparison between the reconstructed and the experimental c_P are presented in Figure 6 and 7. To better assess the proposed technique by comparison with a standard pressure-retrieval method, the solution of the Poisson equation in its conservative formulation (Method A of section 3.3) with full Neumann boundary conditions was purposely implemented by means of finite differences. A second-order centred approximation of the derivatives was adopted in the domain while second-order sided differences were employed on the boundary. The c_P distribution comparison between the two techniques is represented in Figures 6f and 7e. Moreover the reconstructed pressure coefficients for Case 1 obtained by means of the proposed technique are compared with those obtained using the Bernoulli equation and a standard panel method (Xfoil) in Figure 6e.

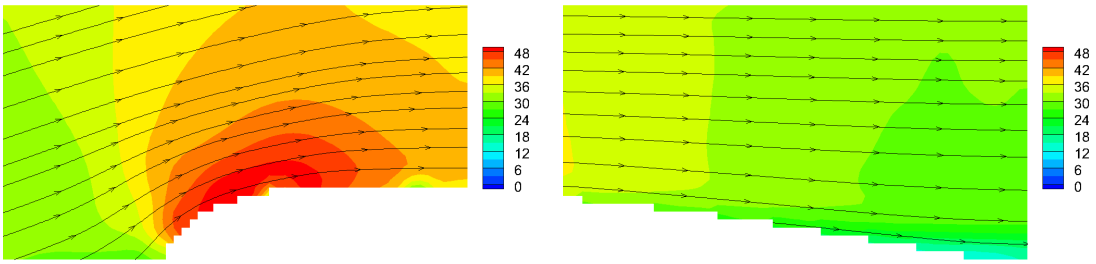

(a) *Leading edge: Velocity field* $[m/s]$ (b) *Trailing edge: Velocity field* $[m/s]$

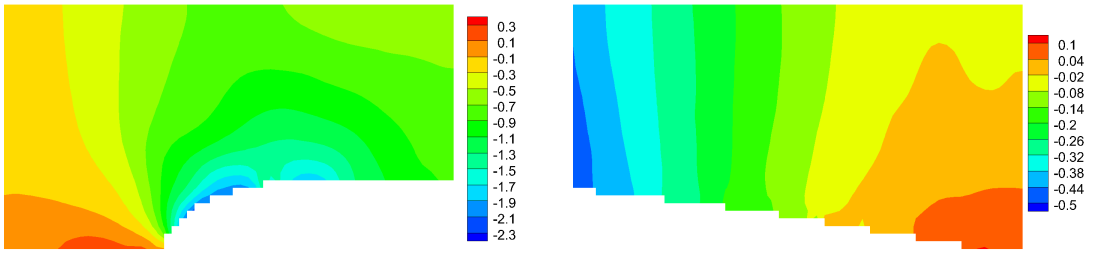

(c) *Leading edge: Reconstructed* c_P (d) *Trailing edge: Reconstructed* c_P

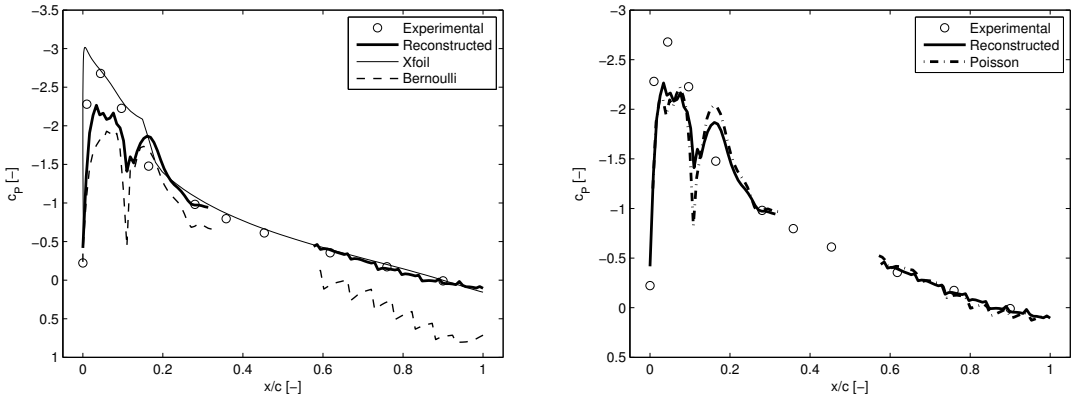

(e) c_P *distribution comparison: Experimental data, Proposed method, Xfoil* (f) c_P *distribution comparison: Experimental data, Bernoulli Theorem and Poisson method*

Fig. 6: Case 1, fixed airfoil test case, $\alpha = 9°$. Input velocity field, (a) and (b), reconstructed c_P field, (c) and (d), and c_P distribution comparison, (e) and (f).

Referring to Fig. 6e and 7e, fairly good agreement is obtained between experimental data and numerical results in most of the test cases, thus providing an assessment of the effectiveness of the proposed technique. Nevertheless, in some cases, the computed pressure value reveals some discrepancies from the corresponding measurement. These discrepancies can be ascribed to three main sources of error, namely:

1. the distance between the points where the pressure is computed and the actual position of the airfoil surface, especially when strong normal pressure gradients are present. This fact does not allow the method to completely resolve the pressure peak at the airfoil leading edge, as highlighted in Figure 7e.

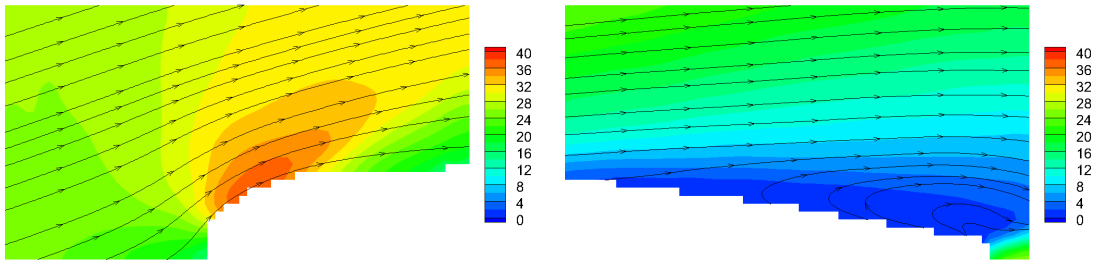

(a) *Leading edge: Velocity field* $[m/s]$ (b) *Trailing edge: Velocity field* $[m/s]$

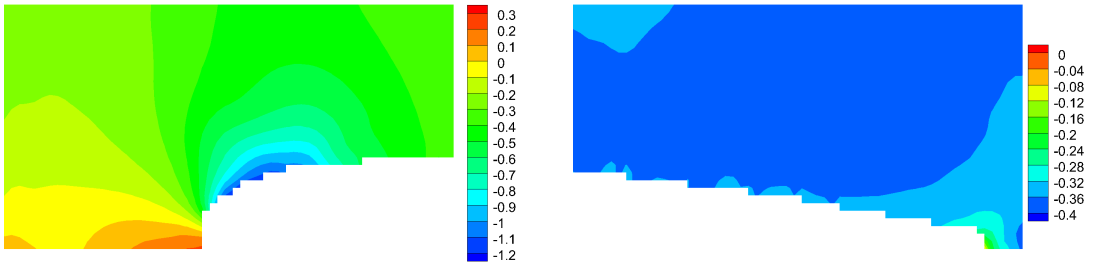

(c) *Leading edge: Reconstructed* c_P (d) *Trailing edge: Reconstructed* c_P

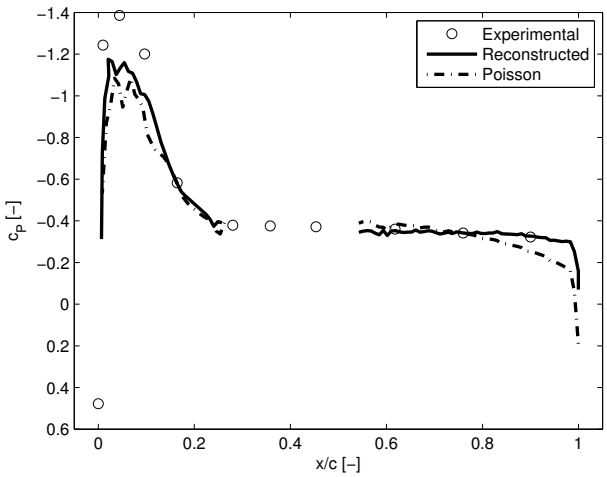

(e) c_P *distribution comparison: Experimental data, Proposed method and Poisson method*

Fig. 7: Case 2, oscillating airfoil test case, $\alpha_0 = 10°$, $A = 10°$, $\alpha = 10°$ downstroke. Input velocity field, (a) and (b), reconstructed c_P field, (c) and (d), and c_P distribution comparison (e).

2. the reduced reliability of the PIV measurements close to the airfoil surface especially where severe light scattering occurs. Light scattering was an issue especially on the leading edge of the airfoil, producing unphysical velocity measurements close to the wall and, therefore, a computed pressure field affected by the same unphysical behaviour. This is well illustrated in Fig. 6a, where an unphysical local velocity minimum can be observed in the region of maximum velocity near the leading edge. This erroneous velocity sample translates in a local maximum of pressure (Fig. 6c). The same effect can be appreciated in the pressure coefficients computed by means of the Bernoulli equation in Figure 6e.

3. the FEM sensitivity to mesh quality, especially with respect to sharp corners on the boundary, see for instance the small oscillations of the reconstructed pressure in correspondence of the mesh corner on the trailing edge in Fig. 6e.

Let us now focus on the comparison between the different pressure-retrieval methods. As it can be appreciated in Figure 6e, the employment of the Bernoulli equation gives fairly good results on the leading edge, where the hypothesis of the theorem can be considered to be verified in the inner nodes due to the thin boundary layer. However it fails in correctly reconstructing the pressure on the trailing edge since the nodes closest to the airfoil lie in the boundary layer, where the irrotationality hypothesis is not verified. For what concerns the comparison between the proposed technique and the classical Poisson formulation of Figures 6f and 7e, they show similar results, with a general better behaviour of the proposed technique with respect of the standard one.

5.2 Time-resolved database

In order to better assess its properties, the proposed technique was also applied to a time-resolved database, where the error is not filtered by the averaging procedure. Two different instantaneous velocity fields were considered, that from now on will be addressed as "Attached" and "Separated" case:

Attached $\alpha_{\text{local}} = 15.8°$ in the upstroke phase of the oscillating motion, just before separation occurs on the upper surface of the trailing edge.
Separated $\alpha_{\text{local}} = 17.2°$ in the upstroke phase of the oscillating motion, as the flow starts to separate from the trailing edge of the airfoil upper surface.

The pressure fields were reconstructed using central differences for the time derivative approximation, as it proved to lead to more accurate results in section 3.3. The input velocity fields are shown in Figure 8a (Attached) and 9a (Separated), the reconstructed c_P fields are shown in Figure 8b (Attached) and 9b (Separated), while the comparison of pressure coefficients reconstructed by the proposed technique and by the standard Poisson formulation are shown in Figure 8c (Attached) and 9c (Separated). In order to fix the pressure offset, the c_P was set equal to the measured one in one of the nodes near the pressure taps.

As it can be appreciated from Figures 8c and 9c, the pressure field was reconstructed very well on most of the airfoil surface, except on the leading edge where the suction peak could not be resolved due to the distance of the measure points from the airfoil surface in a region where strong normal pressure gradients are present, as already pointed out in the section 5.1. This fact was confirmed by comparison with CFD simulations for the same configuration. The CFD-computed pressure coefficients were extracted in the points corresponding to the PIV measurement points closest to the airfoil surface. The results near the airfoil nose were comparable with those reconstructed by means of the proposed technique, thus confirming that this effect can be held accountable for the encountered discrepancy.

In addition, the point of flow-separation is correctly captured, as it can be appreciated from the slight pressure variation in Figure 9c at approximately $x/c = 0.6$. For what concerns the comparison between the proposed technique and the Poisson method, an overall better performance of the proposed method can be appreciated in both figure 8c and 9c.

6 Conclusions

In this work, an innovative and accurate procedure to compute the pressure field from PIV velocity measurements has been proposed based on the uncoupling of the velocity and pressure fields in the incompressible Navier–Stokes equations which relies on exact integral conditions for the pressure. By means of the Glowinski and Pironneau (1979) method, a set of linear PDE problems for the unknown pressure field has been derived and its numerical solution has been implemented by the finite-element method.

First the proposed method is tested against an exact solution of the Navier–Stokes equations over a square domain, showing second order accuracy with respect to the grid size h, the pressure

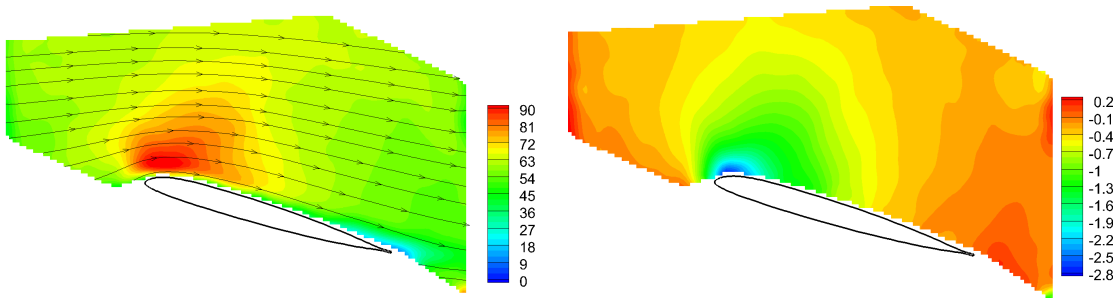

(a) *Velocity field* $[m/s]$ (b) *Reconstructed* c_P *field*

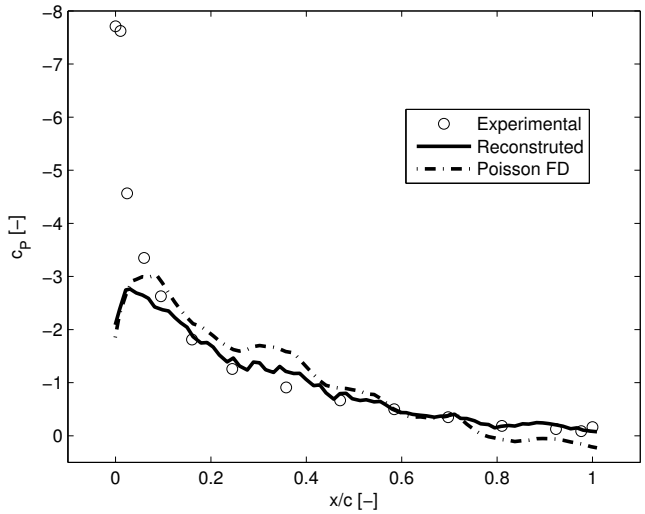

(c) c_P *distribution comparison: Experimental data, Proposed method, Poisson method*

Fig. 8: Time-resolved database: Attached case. Oscillating airfoil at $\alpha_{\text{local}} = 15.8°$ upstroke. Input velocity field (a), reconstructed c_P field (b), and c_P distribution comparison (c).

error being computed in the L^∞ norm. This norm has been chosen because it gives valuable information to appraise the properties of the method from the viewpoint of the experimentalist. Moreover, Monte Carlo simulations, with imposed stochastic perturbations of the velocity field, show that the regions that are most sensitive to the error on the velocity data are the boundary and the corners of the domain, with an approximate ratio between the standard deviation of the error and the standard deviation of the perturbation of almost 2, for the present test case. This ratio is quite insensitive to a change in the perturbation amplitude.

The performance of the proposed method has been also compared with that provided by other methods exploiting the test case proposed by Charonko et al (2010). The comparison shows a remarkable smoothing of the velocity error, that allows the proposed method to be significantly more accurate than the other techniques proposed so far.

Finally, the method has been applied to both phase-averaged and time-resolved PIV measurements of a challenging aeronautical problem: the oscillating airfoil. The comparison between the computed pressure distribution and the available pressure measurements on the airfoil surface shows pretty encouraging results. The reconstructed pressure field presents the expected structures of the examined cases (e.g separated flow, reattaching flow, etc.). Nevertheless some discrepancies are still present between the reconstructed and the experimental pressure values. These discrepancies can be ascribed more to the limitations of the PIV measurements than to the method itself. In particular, the fact that the boundary nodes are quite distant from the airfoil surface where the reference pressure is measured, and the scattering of the laser sheet near the airfoil leading edge.

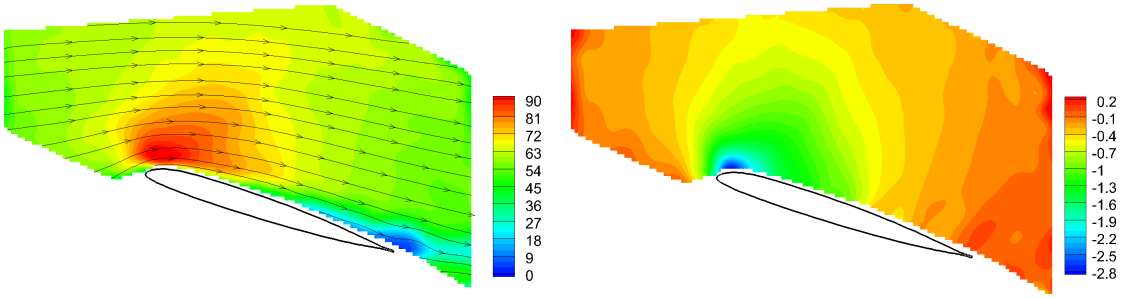

(a) *Velocity field* $[m/s]$ (b) *Reconstructed* c_P *field*

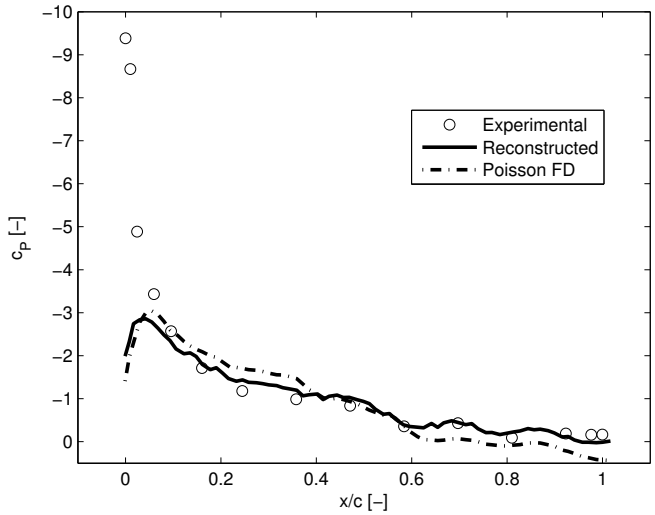

(c) c_P *distribution comparison: Experimental data, Proposed method, Poisson method*

Fig. 9: Time-resolved database: Separated case. Oscillating airfoil at $\alpha_{\text{local}} = 17.2°$ upstroke. Input velocity field (a), reconstructed c_P field (b), and c_P distribution comparison (c).

Moreover direct comparison with the Poisson method for the pressure field reconstruction showed an overall better performance of the proposed method.

Acknowledgements The authors gratefully thank Prof. Luigi Quartapelle for his contribution to the formulation and numerical implementation of the proposed method.

Appendix A: Treatment of pressure Dirichlet boundary conditions

When reliable pressure measurements are available, Dirichlet boundary conditions for the pressure variable can be enforced in that part of the boundary. The starting problem is the following:

$$\begin{cases} \dfrac{\partial \boldsymbol{U}}{\partial t} + (\boldsymbol{U}\cdot\boldsymbol{\nabla})\boldsymbol{U} - \nu\nabla^2\boldsymbol{U} + \boldsymbol{\nabla}P = \boldsymbol{F} & \text{in} \quad V, \\ \boldsymbol{\nabla}\cdot\boldsymbol{U} = 0, & \\ \boldsymbol{U} = \boldsymbol{B} & \text{on} \quad S_U, \\ P = \bar{P}, \quad \boldsymbol{U}\cdot\boldsymbol{n} = \boldsymbol{B}\cdot\boldsymbol{n}, \quad \frac{\partial(\boldsymbol{U}\cdot\boldsymbol{\tau})}{\partial n} = \beta & \text{on} \quad S_P, \end{cases} \tag{24}$$

where S_P is the portion of the boundary where pressure measurements are available, while in S_U the velocity measurement is only available, in such way that $S_P \cup S_U = S$. The new uncoupled formulation reads:

$$\begin{cases} -\nabla^2 p = -\boldsymbol{\nabla}\cdot\boldsymbol{g}, & p|_{S_P} = \bar{p}, & & \\ (-\nabla^2 + \gamma\vartheta)\boldsymbol{v} = -\boldsymbol{\nabla}p + \boldsymbol{g}, & \boldsymbol{v}|_{S_U} = \boldsymbol{b}, & \boldsymbol{v}\cdot\boldsymbol{n}\big|_{S_P} = \boldsymbol{b}\cdot\boldsymbol{n}, & \frac{\partial(\boldsymbol{v}\cdot\boldsymbol{\tau})}{\partial n}\big|_{S_P} = \beta, \\ -\nabla^2\varphi = \boldsymbol{\nabla}\cdot\boldsymbol{v}, & \varphi\big|_S = 0, & \frac{\partial\varphi}{\partial n}\big|_S = 0. & \end{cases} \tag{25}$$

By introducing decomposition (7), one obtains the following sets of equations:

$$\begin{cases} -\nabla^2 p^0 = -\boldsymbol{\nabla}\cdot\boldsymbol{g}, & p^0|_{S_U} = 0, & p^0|_{S_P} = \bar{p}, & \\ (-\nabla^2 + \gamma\vartheta)\boldsymbol{v}^0 = -\boldsymbol{\nabla}p^0 + \boldsymbol{g}, & \boldsymbol{v}^0|_{S_U} = \boldsymbol{b}, & \boldsymbol{v}^0\cdot\boldsymbol{n}\big|_{S_P} = \boldsymbol{b}\cdot\boldsymbol{n}, & \frac{\partial(\boldsymbol{v}^0\cdot\boldsymbol{\tau})}{\partial n}\big|_{S_P} = \beta, \\ -\nabla^2\varphi^0 = \boldsymbol{\nabla}\cdot\boldsymbol{v}^0, & \varphi^0|_S = 0, & & \end{cases} \tag{26}$$

$$\begin{cases} -\nabla^2 p^k = 0, & p^k|_{S_U} = \mu^k, & p^k|_{S_P} = 0 & \\ (-\nabla^2 + \gamma\vartheta)\boldsymbol{v}^k = -\boldsymbol{\nabla}p^k, & \boldsymbol{v}^k|_{S_U} = 0, & \boldsymbol{v}^k\cdot\boldsymbol{n}\big|_{S_P} = 0, & \frac{\partial(\boldsymbol{v}^k\cdot\boldsymbol{\tau})}{\partial n}\big|_{S_P} = 0, \qquad k = 1:\infty \\ -\nabla^2\varphi^k = \boldsymbol{\nabla}\cdot\boldsymbol{v}^k, & \varphi^k|_S = 0, & & \end{cases} \tag{27}$$

The remaining equations are analogous to those derived in section 2.2, with the distinction that now N_D does not represent the total number of the boundary nodes, but only the number of the nodes belonging to S_U.

A final word of caution for the reader is in order. By partially enforcing Dirichlet boundary conditions for pressure, additional errors may be introduced in the pressure-field reconstruction due to the pressure measurement error. The authors recommend to use the standard formulation of the proposed technique, in which the boundary values are derived from the velocity field, unless highly-reliable pressure measurements are available.

References

Aziz AK, Werschulz A (1980) On the numerical solutions of Helmholtz's equation by the finite element method. SIAM Journal on Numerical Analysis 17(5):681–686

Baur T, Köngeter J (1999) PIV with high temporal resolution for the determination of local pressure reductions from coherent turbulence phenomena. In: 3rd International Workshop on Particle Image Velocimetry,(Santa Barbara, CA, USA),(1999-9)

Berton E, Maresca C, Favier D (2004) A new experimental method for determining local airloads on rotor blades in forward flight. Experiments in fluids 37(3):455–457

Box GE, Muller M (1958) A note on the generation of random normal deviates. The Annals of Mathematical Statistics 29(2):610–611

Charonko J, King C, Smith B, Vlachos P (2010) Assessment of pressure field calculations from particle image velocimetry measurements. Measurement Science and Technology 21(10):105,401

De Kat R, Van Oudheusden B (2012) Instantaneous planar pressure determination from PIV in turbulent flow. Experiments in fluids 52(5):1089–1106

Fujisawa N, Tanahashi S, Srinivas K (2005) Evaluation of pressure field and fluid forces on a circular cylinder with and without rotational oscillation using velocity data from PIV measurement. Measurement Science and Technology 16(4):989

Ghaemi S, Ragni D, Scarano F (2012) PIV-based pressure fluctuations in the turbulent boundary layer. Experiments in fluids 53(6):1823–1840

Gibertini G, Mencarelli A, Zanotti A (2013) Oscillating aerofoil and perpendicular vortex interaction. Proceedings of the Institution of Mechanical Engineers, Part G: Journal of Aerospace Engineering

Glowinski R, Pironneau O (1979) On a mixed finite element approximation of the stokes problem (i). Numerische Mathematik 33(4):397–424

Guermond J, Quartapelle L (1998) On stability and convergence of projection methods based on pressure Poisson equation. International Journal for Numerical Methods in Fluids 26(9):1039–1053

Gurka R, Liberzon A, Hefetz D, Rubinstein D, Shavit U (1999) Computation of pressure distribution using PIV velocity data. In: Workshop on Particle Image Velocimetry

Liu X, Katz J (2006) Instantaneous pressure and material acceleration measurements using a four-exposure PIV system. Experiments in Fluids 41(2):227–240

Obi S, Tokai N (2006) The pressure–velocity correlation in oscillatory turbulent flow between a pair of bluff bodies. International journal of heat and fluid flow 27(5):768–776

Panciroli R, Porfiri M (2013) Evaluation of the pressure field on a rigid body entering a quiescent fluid through particle image velocimetry. Experiments in Fluids 54(12):1–13

Quartapelle L (1993) Numerical solution of the incompressible Navier–Stokes equations, vol 113. Springer

Quartapelle L, Napolitano M (1986) Integral conditions for the pressure in the computation of incompressible viscous flows. Journal of Computational Physics 62(2):340–348

Ragni D, van Oudheusden B, Scarano F (2012) PIV-load determination in aircraft propellers. In: 16th Inernational Symposium on Applications of Laser Techniques to Fluid Mechanics,(Lisbon, Portugal),(2012-7)

Van Oudheusden B (2013) PIV-based pressure measurement. Measurement Science and Technology 24(3):032,001

Van Oudheusden BW, Scarano F, Roosenboom E, Casimiri E, Souverein L (2007) Evaluation of integral forces and pressure fields from planar velocimetry data for incompressible and compressible flows. Experiments in Fluids 43(2-3):153–162

Violato D, Moore P, Scarano F (2011) Lagrangian and eulerian pressure field evaluation of rod-airfoil flow from time-resolved tomographic PIV. Experiments in fluids 50(4):1057–1070

Zanotti A (2012) Retreating blade dynamic stall. PhD thesis, Politecnico di Milano

Zanotti A, Gibertini G (2012) Experimental investigation of the dynamic stall phenomenon on a NACA 23012 oscillating airfoil. Proceedings of the Institution of Mechanical Engineers, Part G: Journal of Aerospace Engineering